# Three-Dimensional Reconstruction of Planar Deformation Features from Single Electron Micrographs

F.D. LEÓN-CÁZARES, C. KIENL, and C.M.F. RAE

Dislocations are crystal defects responsible for plastic deformation, and understanding their behavior is key to the design of materials with better properties. Electron microscopy has been widely used to characterize dislocations, but the resulting images are only two-dimensional projections of the real defects. The current work introduces a framework to determine the sample and crystal orientations from micrographs with planar deformation features (twins, stacking faults, and slip bands) in three or four non-coplanar slip systems of an fcc material. This is then extended into a methodology for the three-dimensional reconstruction of dislocations lying on planes with a known orientation that can be easily coupled with a standard Burgers vector analysis, as proved here in a nickel-based superalloy. This technique can only be used in materials that show specific deformation conditions, but it is faster than other alternatives as it relies on the manual tracing of dislocations in a single micrograph.

© The Author(s) 2019

## I. INTRODUCTION

MULTIPLE electron microscopy techniques allow the visualization of plastic deformation features such as dislocations, stacking faults, and twins. However, the resulting micrographs are two-dimensional (2D) projections of the underlying structures. Information regarding the depth of these features can be inferred within a transmission electron microscope (TEM), but the true three-dimensional (3D) geometry remains hidden due to the nature of the technique. Elaborate methodologies have been built to recreate the real shape of the deformation features, motivated by the need to understand the complex deformation mechanisms taking place in crystalline materials. However, these tools are typically time-consuming and labor-intensive. The current study aims to minimize the time and work required to obtain a realistic model of the region imaged for the case of fcc crystals where the deformation features are planar in nature.

Some of the 3D reconstruction techniques from the literature are discussed first to offer a wider perspective of the alternatives. The scanning electron microscope (SEM) serial sectioning method uses electron channeling contrast imaging (ECCI) at a surface of the sample to observe dislocations with a backscattered detector. Alternating focused ion beam to remove a layer of material with imaging of the sample results in sequential planar datasets that can be then combined to form a 3D model.[1] This technique appears to be scalable for analyses at the micrometer length scale, although being a labor-intensive destructive technique limits its applicability. The same disadvantage goes to atom probe tomography (APT), a chemistry-sensitive technique with atomic resolution in which the locations of up to 60 pct of the atoms in a thin needle of material are traced as it is evaporated.[2]

Electron tomography is a well established technique in which tenths or hundreds of TEM images manually focused and with a similar reciprocal-lattice **g**-vector are taken at short tilt intervals.[3–5] The variation in contrast for the different orientations is corrected *via* image processing before the data acquired are merged *via* a sequentially iterated reconstruction technique. The resolution obtained depends on the sample characteristics and magnification used, and it may go up to atomic resolution for small volumes (~ 2 nm).[6] Nonetheless, heavy computational requirements, long imaging times, and good sample conditions are drawbacks of the technique. Ferromagnetism in steel samples is an additional limitation, although improved sample preparation and imaging techniques have circumvented this problematic.[7] The use of scanning TEM (STEM) and automated image acquisition and processing have significantly improved electron tomography,[8] but it still involves a considerable amount of work. However, a

F.D. LEÓN-CÁZARES, C. KIENL, and C.M.F. RAE are with the Department of Materials Science & Metallurgy, University of Cambridge, 27 Charles Babbage Rd, Cambridge, CB3 0FS, UK. Contact e-mail: fdl22@cam.ac.uk

newly developed tilt-less tomography technique drastically reduced the required microscopy time by effectively rotating the electron beam within STEM instead of the sample, followed by a dedicated reconstruction algorithm.[9]

Dislocation reconstruction from stereo pairs of electron micrographs avoids some of the aforementioned complexities by imitating the way in which animals perceive depth.[10] Two views of the same region at different orientations result in a depth-dependent displacement of the features, also known as parallax, from which a three-dimensional perspective can be formed. In the case of TEM, the dislocations will have the same visibility in both images if they have identical diffraction conditions, which allows for a 3D impression of their geometry if the stereo pair is combined into an anaglyph and seen with special colored glasses.[11] McCabe et al.[12] and more recently Agudo-Jacome et al.[13] have created 3D reconstruction methodologies based on tracing segments of the dislocations on both micrographs and matching them together accounting for the parallax at each point.

Alternatively, this work employs knowledge about the orientation of the sample and the deformation mechanisms of a specific crystal structure to facilitate the 3D reconstruction task. Plastic deformation in fcc materials occurs mostly along the octahedral {111} planes in the form of dislocation glide, pile-ups, slip bands, persistent slip bands, extended intrinsic and extrinsic stacking faults, and twinning, among others. Glissile dislocations are then constrained to lie in one of four possible slip plane orientations and consist of dislocations with $\frac{a}{2}\langle 110 \rangle$ or $\frac{a}{6}\langle 112 \rangle$ Burgers vectors defined by Thompson's tetrahedron.[14] All these known constraints limit the number of configurations in which the features may look in a micrograph and can then be used when rationalizing the possible dislocation mechanisms that take place in the material.

The current work introduces two main techniques. The first one deals with methods to obtain the orientation of a crystal with respect to the view plane via a geometric analysis of the intersections between some octahedral planes and the sample surface. Different scenarios in which this technique can be used are discussed for samples with or without a tilt with respect to the electron beam, both for SEM and TEM. The second one is a methodology extended from this framework to reconstruct a realistic 3D view of the dislocations within a TEM sample from their 2D projections onto a micrograph. Deformed nickel-based superalloys are used for experimental validation.

## II. OBTAINING THE CRYSTAL ORIENTATION

A general simplified geometry of the sample and the electron beam needs to be introduced to facilitate the calculation of the crystal orientation from both SEM and TEM micrographs. Consider the setup in Figure 1(a) in which the projected image building a micrograph lies directly below the sample so that a pixel contains the information of the atoms directly above it. The lenses in the electron microscope are omitted for simplicity. Position then an orthonormal right-handed coordinate system oriented so that the z-axis is parallel to the electron beam and the x and y axes coincide with the horizontal and vertical edges of the acquired 2D micrograph. Thus, only the (x,y) coordinates of every feature are directly accessible. In the case of an SEM, a plane describing the sample surface with normal $\mathbf{n_s} = (a_s, b_s, c_s)$ will be parallel to the electron beam when $a_s = b_s = 0$ and $c_s \neq 0$, where all the coefficients are real numbers. For the TEM, lets assume an ideal case where the imaged region of the sample has a constant thickness $t$ and the top surface has a normal vector $\mathbf{n_s}$ (with $c_s \geq 0$), as shown in Figure 1(a). The effects of this assumption are further discussed in Section V. Moreover, no bending of the crystal lattice is considered.

A full description of the orientation of an fcc crystal can be given by defining the equations of two out of the four octahedral planes forming Thompson's tetrahedron. Similar to the sample plane, these are given by their normals $\mathbf{n_i} = (a_i, b_i, c_i)$, where the subindex $i = 1, 2, 3, 4$ corresponds to each plane orientation. Taking these to be unit vectors, i.e.,

$$|\mathbf{n_i}| = \mathbf{1}, \quad [1]$$

these parameters are further constrained independently of the sample setup by

$$\mathbf{n_i} \cdot \mathbf{n_j} = -\cos\phi \quad [2]$$

for $i \neq j$, where $\phi = \arccos(1/3)$ is the dihedral angle of a regular tetrahedron.

The intersection $\mathbf{v_i} = (v_x, v_y, v_z)$ between the sample plane and plane $i$ obtained by the cross product $\mathbf{v_i} = \mathbf{n_s} \times \mathbf{n_i}$ defines the line that plastic deformation features will form upon reaching the surface of the sample. Ignoring the z-coordinate of such vector results in its 2D projection onto the view plane, from which its slope

$$m_i = \frac{c_s a_i - a_s c_i}{b_s c_i - c_s b_i} \quad [3]$$

and angle $\theta_i = \arctan(m_i)$ can be measured, as seen in Figure 1(b).

Similarly, the width of the projections of these features onto the view plane can be used to determine the orientation of the crystal within the TEM. This stems from the fact that the intersections of a plane with both sample surfaces are two parallel lines, as shown in Figure 1. The 2D spacing between the projections of these intersections onto the view plane is a distance that can be easily measured in a micrograph. The separation $w$ between two parallel lines in the form $y = mx + b$ is

$$w = \frac{|b_{II} - b_I|}{\sqrt{1 + m^2}}, \quad [4]$$

where $b_I$ and $b_{II}$ are the independent terms of each line.[15] Consequently, the equations of both intersections are sought.
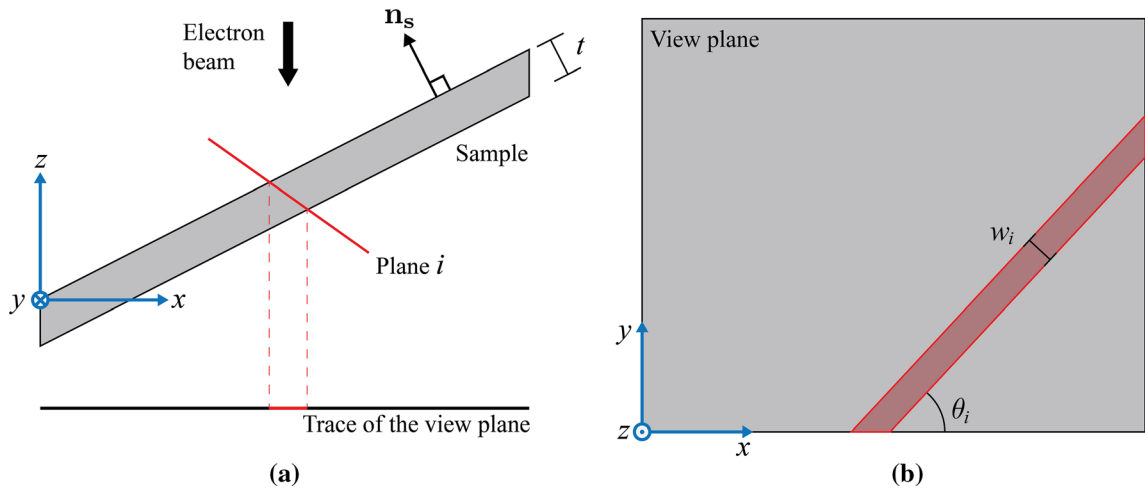
Fig. 1—(a) Lateral view of the simplified setup with the micrograph directly below the sample imaged, being crossed by slip plane i (red). Note that the tilt axis and the y-axis do not have to be aligned necessarily. (b) Schematic of the resulting micrograph with the projection of such feature onto the view plane. Refer to Section II for a more detailed description of the adopted setup (Color figure online).

Placing a point of one of the sample surfaces at the origin of the coordinate system makes the equation of the second plane

$$a_s x + b_s y + c_s z + t = 0 \qquad [5]$$

for a unit normal vector. To obtain the equation of the intersection between this and plane i, it is required to obtain a point $P_0 = (x_0, y_0, z_0)$ that belongs to it. Solving the equations

$$a_s x_0 + b_s y_0 + c_s z_0 + t = 0 \qquad [6a]$$

$$a_i x_0 + b_i y_0 + c_i z_0 = 0 \qquad [6b]$$

by setting $z_0 = 0$ yields

$$x_0 = \frac{-t b_i}{a_s b_i - b_s a_i} \qquad [7a]$$

$$y_0 = \frac{t a_i}{a_s b_i - b_s a_i}. \qquad [7b]$$

Plugging [7a] and [7b] into the symmetric equation of the intersection on the $xy$ plane

$$\frac{x - x_0}{v_{ix}} = \frac{y - y_0}{v_{iy}}, \qquad [8]$$

solving for $y$ and substituting into Eq. [4] leads to

$$w_i = \frac{t \left| \frac{c_i}{b_s c_i - c_s b_i} \right|}{\sqrt{1 + \left( \frac{-a_s c_i + c_s a_i}{b_s c_i - c_s b_i} \right)^2}}. \qquad [9]$$

The widths of the projection of the features are as expected directly proportional to the thickness of the sample. If the orientations of the crystal and the sample are known, Eq. [9] can also be used to determine the thickness of the sample.

If all the parameters for two octahedral planes are known, the equations for the third and fourth planes are the only two real solutions to the system of equations

$$|\mathbf{n_3}| = 1 \qquad [10a]$$

$$\mathbf{n_1} \cdot \mathbf{n_3} = -\cos \phi \qquad [10b]$$

$$\mathbf{n_2} \cdot \mathbf{n_3} = -\cos \phi. \qquad [10c]$$

Furthermore, the rotation matrix $R$ to access the crystal coordinates can be obtained by solving a linear system of equations for the components of three vectors known in both coordinate systems. In this case these vectors are the intersections between three slip planes $\mathbf{v_{12}} = \mathbf{n_1} \times \mathbf{n_2}$, $\mathbf{v_{23}} = \mathbf{n_2} \times \mathbf{n_3}$ and $\mathbf{v_{31}} = \mathbf{n_3} \times \mathbf{n_1}$, and the system of equations can be constructed from $R\mathbf{v_{12}} = [011]$, $R\mathbf{v_{23}} = [110]$ and $R\mathbf{v_{31}} = [101]$. All that is left is then to obtain the equations for two or more octahedral slip planes.

There are different scenarios for putting this into practice. Consider firstly that in which the orientation of the sample surface is known. This is in general common for SEM or for TEM (with the aforementioned assumption regarding an ideal sample) if the tilt angles of the sample holder are known. It is possible to obtain the sample normal by applying the corresponding Tait-Bryan chained rotations to a $(0, 0, 1)$ vector respective axes. Deformation features on three non-parallel octahedral slip planes are required to get the crystal orientation in this case, accounting for nine variables. The corresponding nine polynomial equations include: Eq. [1] for each plane, Eq. [2] for their dihedral angles and Eq. [3] for their corresponding projections onto the view plane.

Secondly, if the orientation of the sample surface is unknown, the three components of its unit normal are added to the list of variables. In this scenario it is possible to incorporate equations via the ratios of the widths of the projections $w_i/w_j$, which may be

determined directly from the micrograph even without knowing the thickness of the sample. Another advantageous configuration that frequently appears in TEM Burgers vector analyses is the presence of an edge-on octahedral plane. This occurs when the reciprocal-lattice **g**-vector of a $\{111\}$ plane lies perpendicular to the electron beam.[16] Under this setup, the 2D slope of the intersection between such edge-on plane (subindex $e$) and the view plane is

$$m_e = \frac{-a_e}{b_e}, \qquad [11]$$

and $c_e = 0$. This effectively gives the normal for that plane and reduces the total number of equations required by one.

A numerical solver for the systems of equations was implemented in a Matlab script. The polynomial nature of these equations leads to multiple solutions, from which only the real ones are taken into account. Some of these are geometrically equivalent, e.g., two solutions with an opposite sign for all the variables. Depending on the input slopes, there are typically one or two different solutions. Among these it is possible to identify which one corresponds to the correct orientation either via the angle $\theta_4$ of the projection of the intersection between the fourth slip plane and the sample surface onto the view plane or by looking at the ratios between the projected widths of the different octahedral planes.

## III. 3D RECONSTRUCTION OF DISLOCATIONS

In order to reconstruct the 3D geometry of a planar feature from its two-dimensional projection it is necessary to know to which plane it belongs, in addition to the $z$-coordinate of at least one point. For a feature $j$ on a plane orientation $i$, this means obtaining the independent term $d_j$ in the equation of its plane $a_ix + b_iy + c_iz + d_j = 0$. Once again consider the coordinate system introduced in Figure 1 with its origin fixed at a point on the top sample surface directly above the bottom left corner of the micrograph on the view plane (or any other point of convenience).

Identifying the plane orientation on which a feature lies may be done from the angle $\theta_i$ of its intersection with the sample surface or by the width of its projection onto the view plane. This task is simple for extended planar faults such as twin boundaries, stacking faults, and even dislocation pile-ups, but may be harder for single dislocations. Imaging a region of a TEM sample for different sample orientations helps to distinguish the slip plane orientation of some of these features by looking at the change in the shape of their projections. This is analogous to performing an analysis to identify the Burgers vectors **b**, and can thus be performed in parallel to it. This work only includes plastic deformation in octahedral planes, but an extension to cubic planes could be incorporated in a similar fashion.

Determining the independent term $d_j$ of a feature can be done from an anchor point $P_{sj} = (x_j, y_j, z_j)$ which lies at the intersection between two planes, even without any information regarding the $z$-coordinates. Solving from equations

$$a_sx_j + b_sy_j + c_sz_j + d_s = 0 \qquad [12a]$$

$$a_ix_j + b_iy_j + c_iz_j + d_j = 0, \qquad [12b]$$

where $d_s$ equals 0 or $t$ depending on which sample surface this point belongs to, yields

$$d_j = -a_ix_j - b_iy_j + \frac{c_i}{c_s}\left(a_sx_j + b_sy_j + d_s\right). \qquad [13]$$

In a similar fashion, the thickness of the sample can be determined if points at the intersections of plane $i$ with both sample surfaces are known. Note that if the wrong value of $d_s$ is chosen then the deformation feature will appear to be extending in the wrong direction from point $P_{sj}$ and thus needs to be fixed.

The reconstruction of a deformation feature can be performed once the equation of its plane is known. Extended defects such as twin boundaries and stacking faults can be drawn as the region of such plane in-between the two sample surfaces, as shown in Figure 2(a). Thus, only the coordinates of one point are required. An individual dislocation can be traced from its $(x, y)$ projection onto the view plane and its $z$-coordinate extracted from the equation of its slip plane. An example of this is given in Figure 2(b). Note then that the resolution of this technique will be that of the micrograph from which the features are drawn.

Another situation analyzed in this work is that of a dislocation changing its slip plane, such as what happens during a cross slip event. After determining the plane of the first segment, it is possible to get the coordinates of point $P_c$ at which the dislocation changes plane. Analogous to Eqs. [12a] and [12b], the independent term of the cross slip plane can be obtained by evaluating both surfaces at point $P_c$. An example of this construction is shown in Figure 2(c). In this way, a continuous dislocation that changes slip planes can be traced in three dimensions while it remains within the TEM sample. Any kind of dislocation node associated to planar defects may be analyzed in this way as long as it is visible in the micrograph.

## IV. MATERIALS AND METHODS

The orientation model was validated with a series of ECCI images in samples of the polycrystalline nickel-based superalloy RR1000. These belonged to specimens that were low cycle fatigued at 20 °C and 700 °C; more information regarding these samples is discussed elsewhere.[17] The ECCI micrographs were taken with a 0 deg tilt in a FEI NOVA NanoSEM after standard sample preparation. Images of 11 grains where stacking faults, twin boundaries or slip bands appeared in four different slip plane orientations were selected for the analysis and the angle $\theta$ of their intercepts with the sample surface were manually recorded. Three of these angles chosen at random were fed into a system of nine

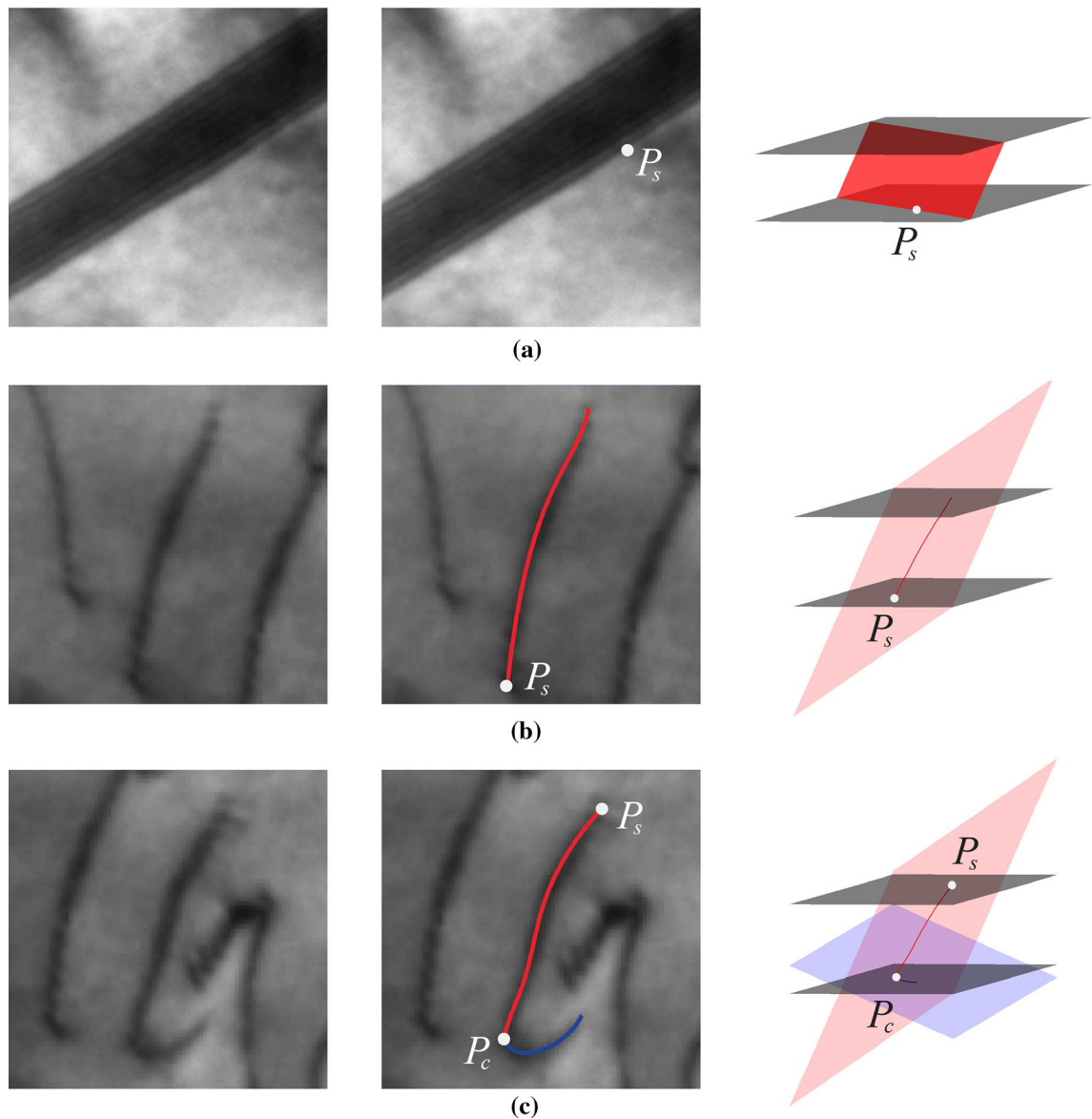Fig. 2—Examples of (*a*) a twin boundary, (*b*) a dislocation, and (*c*) a cross slip event as seen in a TEM micrograph, traced on their view planes and reconstructed into 3D models shown as orthographic projections (from left to right). The Points $P_s$ and $P_c$ lie at a sample surface and a cross slip plane, respectively. Drawing the dislocations requires tracing every point along their lengths, whereas only one point is needed for a planar extended fault. Relevant slip planes are drawn for reference in the 3D model and colored to match the deformation features that lie on them (Color figure online).

equations for the three plane normals and the predicted value of $\theta_4$ was compared to the measured one.

Alternatively, an electropolished TEM sample was extracted from the nickel-based superalloy ATI 718Plus after an interrupted compression test at 975 °C for a strain of − 1.2 and with a strain rate of 1 s⁻¹. A recrystallized grain with dislocations and twin boundaries was imaged in a JEOL 200CX TEM in bright field mode with an operating voltage of 200 kV. Micrographs at different orientations around a [111] zone axis were accessed with a double tilt holder. The orientations of the sample and slip planes were obtained with a variation of the system of equations presented in Section II (further detailed in Section V). This was followed with a 3D reconstruction of the deformation

features in Matlab. Additional information regarding this sample can be found elsewhere.[18]

## V.  RESULTS AND DISCUSSION

The deformed nickel-based superalloy RR1000 contains many grains with deformation features in all their octahedral planes, including stacking faults, twin boundaries, and slip bands. Figure 3 shows an example of an ECCI micrograph used to calculate the orientation of a grain, with red lines marking the four slip plane orientations. After numerically solving the required system of equations for three of those planes, one or two real solutions were always obtained. The closest

value of $\theta_4$ to the measured fourth orientation is compared to the real value. From the 11 grains analyzed, the mean error recorded is 0.4 deg, the standard deviation 0.3 deg and the maximum error 1 deg (refer to electronic supplementary material). This is an indication of how precise this model can be if the required features appear in a micrograph.
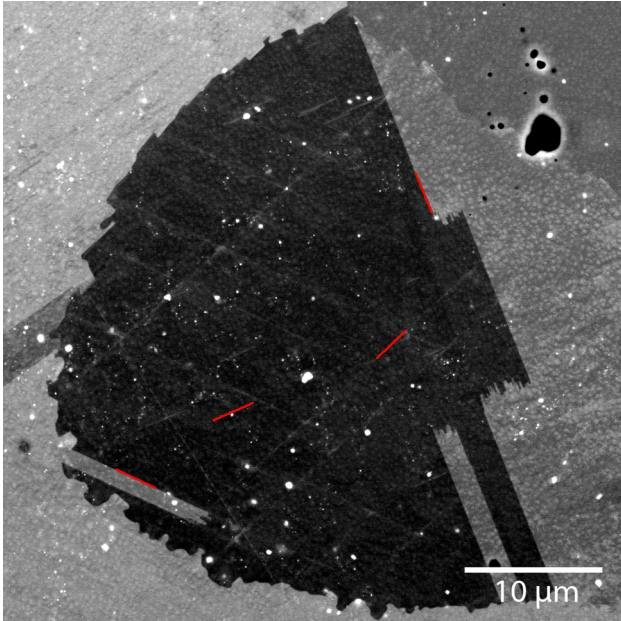


Fig. 3—SEM micrograph of an RR1000 sample showing deformation features in four distinct slip plane orientations highlighted in red (Color figure online).

Figure 4(a) shows one of the TEM micrographs of alloy 718Plus with multiple plastic deformation features, including two non-parallel twin boundaries, numerous perfect dislocations on different slip planes, and Shockley partials bounding intrinsic stacking faults. The **g**-vector drawn corresponds to the $(\overline{1}\overline{1}1)$ plane and lies perpendicular to the electron beam. Even though the tilt angles of the TEM sample holder were recorded, the orientation of the specimen surface could not be directly reproduced from them due to an initial misorientation between the sample normal and the electron beam for an untilted configuration $\alpha = \beta = 0$. Thus, the components of this vector were also sought *via* a system of equations. The parameters describing the edge-on plane $(a_1, b_1, 0)$ are given by Eqs. [1] and [11]. Afterwards, the missing nine variables (the components of the normal vectors $\mathbf{n_s}$, $\mathbf{n_2}$ and $\mathbf{n_3}$) are found with a system of nine equations: (i–iii) Eq. [1] for each unit normal, (iv–vi) Eq. [2] for the dihedral angles between planes 1, 2, and 3, (vii–viii) Eq. [3] for the slopes of the 2D projections of the intersections between the sample surface and both twin boundaries and (ix) a relation of the ratio between the projection widths of both twin boundaries $w_2/w_3$ from Eq. [9]. A solution with $c_s > 0$ is chosen to ensure that the reconstructed geometry corresponds to the setup adopted in Figure 1. Table I summarizes the input and output data of this configuration.

The invisibility criteria associated with the dislocations numbered in Figure 4(a) are summarized in Table II. Note that dislocation 4 is invisible in this micrograph , showing only residual contrast, but visible in others. The Burgers vector analysis constrains the perfect dislocations to lie in one of two possible slip planes. From the direction in which they bow, their intersections with a sample surface and their projected
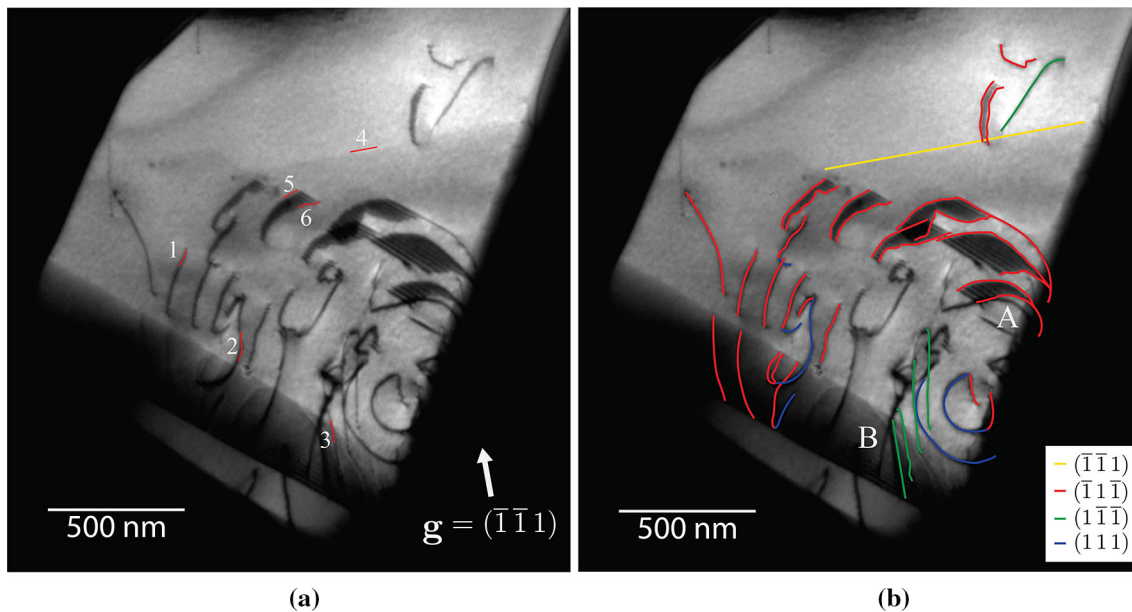


Fig. 4—(a) TEM bright field micrograph of a region with two non-parallel twin boundaries and multiple dislocations. The numbered segments are the dislocations on which the Burgers vector analysis was performed. The $xy$ coordinates of the dislocations are traced in the same image shown in (b), with the different colors indicating the octahedral slip planes in which they are gliding. Regions of interest A and B are marked and further discussed in the text (Color figure online).

widths it is usually possible to determine exactly in which slip plane it glides, as shown in the last column of the table. The analysis of each feature is obtained independently with the exception of the Shockley partials bounding each stacking fault, which are forced to lie on the same plane.

The color-coded tracing of the dislocations in this micrograph is shown in Figure 4(b), with regions of interest denoted with capital letters. In some regions such as A or B it becomes very difficult to trace a dislocation due to poor contrast occurring from nearby defects or because of the proximity of its projection to that of other dislocations. This highlights again the importance of the original micrograph's orientation, resolution and contrast. Upon applying the methodology for the reconstruction of the plastic deformation features, the 3D model depicted in Figure 5 is built.

Note that many realistic characteristics of the model arise without being imposed *a priori*. An example of this is the termination of both ends of all the dislocations at a sample surface or very close to it, even though only one end was fixed at such plane. Besides, the dislocations systematically go further beyond the sample surfaces the more to the left they are in the micrograph. This, together with the slight difference on the slope created by the projection of the intersection between the bottom twin and both sample surfaces, indicates that there is a thickness gradient originated by the electropolishing technique used, with the thinner regions to the right side of the micrograph. The dislocation pile-up in region *B* stopping at the twin boundary is another feature not set *a priori*. A similar situation is that of the dissociated dislocations not going beyond the twin boundary on the right side of the micrograph. These constitute proofs of the validity of the technique.

The micrographs of this grain taken at different orientations can also be reproduced upon rotating the 3D model, as shown in Figure 6. Obviously, the dislocations do not disappear in the reconstruction as no invisibility criterion $\mathbf{g} \cdot \mathbf{b} = 0$ is set, but this option could be easily coupled with the current technique as all the information required for each dislocation is already known. Additionally, the dislocations on planes with a $(\bar{1}\bar{1}1)$ orientation are not reconstructed as these were in an edge-on orientation in the micrograph from which the deformation features were traced.

**Table I. Input and Output Data for the TEM Micrograph Orientation Configuration**

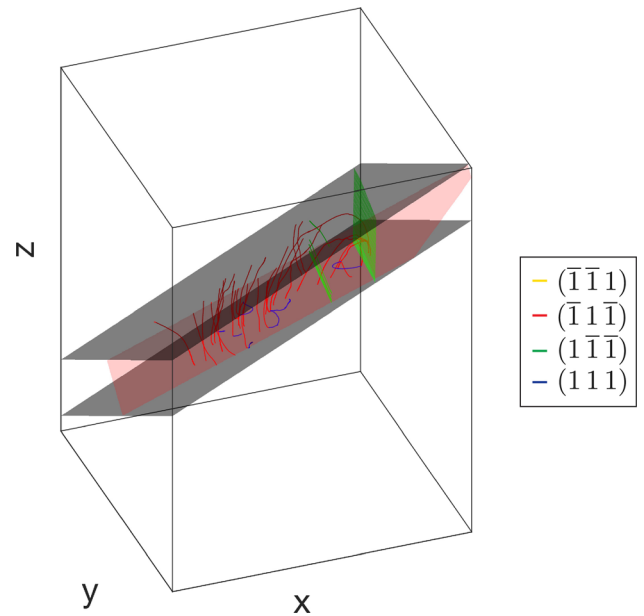| Input Data | |
|---|---|
| $\theta_1$ | 10.3 deg |
| $\theta_2$ | $-$ 28.9deg |
| $\theta_3$ | 69.4 deg |
| $w_2/w_3$ | 1.74 |
| Output Data | |
| $\mathbf{n_s}$ | (0.4, $-$ 0.47, 0.79) |
| $\mathbf{n_1}$ | (0.18, $-$ 0.98, 0) |
| $\mathbf{n_2}$ | (0.7, 0.47, 0.54) |
| $\mathbf{n_3}$ | ($-$ 0.9, 0.18, 0.4) |
| $\mathbf{n_4}$ | ($-$ 0.01, $-$ 0.34, 0.94) |
| $\theta_4$ | 66.32 deg |
| $t$ | 13.68 nm |
| $w_2$ | 10.37 nm |
| $w_3$ | 5.96 nm |
| $w_4$ | 30.4 nm |



Fig. 5—Orthographic projection of a 3D reconstruction of the dislocations (lines) and twin boundaries (planes) within the TEM specimen imaged. The black planes represent the sample surfaces, and the deformation features follow the same color coding used in Fig. 4(b) (Color figure online).

**Table II. Table of Visibility for Different g-Vectors for the Dislocations Numbered in Fig. 4(a); v = visible, w = weak, i = invisible**

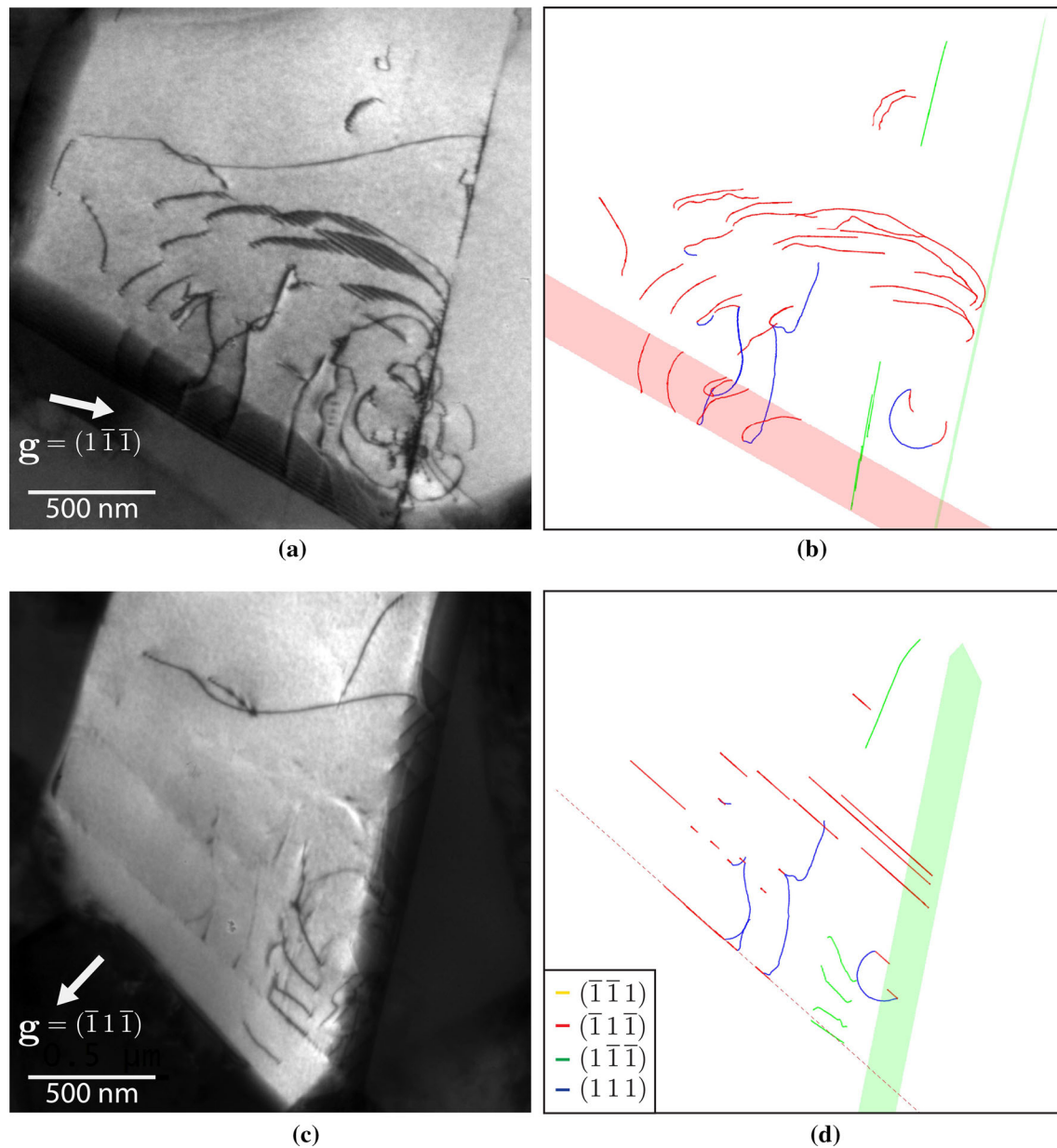| Dislocation | $(\bar{1}\bar{1}1)$ | $(1\bar{1}\bar{1})$ | $(\bar{1}1\bar{1})$ | $(2\bar{2}0)$ | $(20\bar{2})$ | $(0\bar{2}2)$ | Slip Direction | Slip Plane |
|---|---|---|---|---|---|---|---|---|
| 1 | v | v | i | v | v | v | $[10\bar{1}]$ | $(\bar{1}1\bar{1})$ |
| 2 | v | v | i | v | v | v | $[10\bar{1}]$ | $(111)$ |
| 3 | v | i | v | v | v | v | $[01\bar{1}]$ | $(1\bar{1}\bar{1})$ |
| 4 | i | v | v | v | v | v | $[1\bar{1}0]$ | $(\bar{1}\bar{1}1)$ |
| 5 | w | v | i | v | v | w | $[21\bar{1}]$ | $(\bar{1}1\bar{1})$ |
| 6 | v | w | i | w | v | v | $[21\bar{1}]$ | $(\bar{1}1\bar{1})$ |

Fig. 6—TEM micrographs of the same region imaged at different orientations with the (a) $(1\bar{1}\bar{1})$ and (c) $(\bar{1}1\bar{1})$ **g**-vectors perpendicular to the electron beam. Their respective reconstructed projections created by rotating the 3D model to the appropriate viewpoints are shown in (b) and (d). The same color coding of Fig. 4(b) is used here for the dislocations and twin boundaries (Color figure online).

Note that most of the reconstructed dislocations are congruent with their 2D projections in the different micrographs, with small deviations that may arise from the orientation determination or from the tracing stage. The latter arises from the resolution of the micrograph due to the apparent thickness of the dislocation line. Nonetheless, this is deemed less important and can be improved with better imaging conditions.

The calculation of the orientation of the sample and the slip planes may introduce bigger discrepancies if not performed accurately. Compare the real and the reconstructed geometries of a dislocation assuming that the calculated normals to the sample and the slip plane had an initial error, as shown in Figure 7(a). Consider first

the angle $\phi_s$ between the view plane and the sample surface. An error $\Delta\phi_s$ in the calculation of such angle introduces an error $\Delta z_s$ in the projected $z$-coordinates that are not constant throughout the sample, but they increase the further away they are from the origin $O$. For an anchor point $P_s$ at a distance $l_s$ from the origin in the horizontal direction perpendicular to such axis, the error introduced is

$$\Delta z_s = l_s(\tan(\phi_s + \Delta\phi_s) - \tan(\phi_s)). \qquad [14]$$

Similarly, an error $\Delta\phi_i$ in the calculation of the dihedral angle between the view plane and plane $i$ introduces a new error
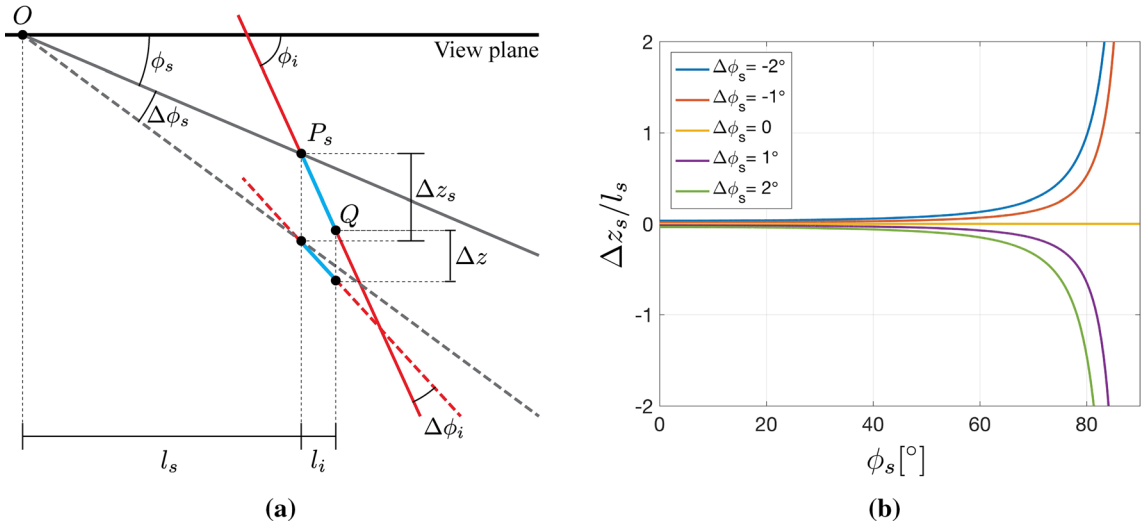
Fig. 7—(a) Schematic diagram of the source of an error in the z-coordinate of point $Q$ of a dislocation (cyan) due to a calculation error in the orientations of the sample (gray) and slip plane $i$ (red). The solid and dashed lines denote the real and calculated planes, respectively. (b) Plots of such depth error as a function of the sample plane orientation (Color figure online).

$$\Delta z_i = l_i(\tan(\phi_i + \Delta\phi_i) - \tan(\phi_i)) \qquad [15]$$

for any point $Q$ of the traced dislocation at a distance $l_i$ from the anchor point. Both of these errors are additive, *i.e.*, the total error introduced is $\Delta z = \Delta z_s + \Delta z_i$. As seen in the plots of Eq. [14] (with the same dependencies for Eq. [15] on $l_i$, $\phi_i$ and $\Delta\phi_i$) for different angles in Figure 7(b), the largest errors arise in planes close to an edge-on orientation. From both deviations $\Delta z_s$ might in general be larger due to the longer distances from the origin to the anchor points. Thus, this error investigation confirms that this technique is better for thinner samples where the projections are usually shorter. Note that the distances $l_s$ and $l_i$ are taken in the direction that would give the highest depth variations, so that all the calculations here realistically represent the higher bounds for the introduced errors.

Overall, this methodology can help rationalizing the deformation behavior of a reconstructed specimen by allowing the user to have a 3D representation of the dislocations rather than their planar projections. Qualitatively, this provides information regarding the dislocation mechanisms. Furthermore, a quantitative investigation is also possible as the true dimensions of the deformation features are acquired with a resolution close to that of the TEM micrograph. The main drawback of the 3D reconstruction technique is the manual nature of identifying the appropriate slip planes of each feature and tracing the (x,y) coordinates of each dislocation. Nonetheless, the applicability and final results of this methodology makes it an attractive post-processing option to characterize deformation behavior.

Compared to other dislocation reconstruction techniques this might be the fastest available for thin samples and low dislocation densities, as it is drawn out of a single micrograph. This makes it a potential tool for complementing standard Burgers vector analysis as it can be recreated from the micrographs typically taken for that, ensuring that the full slip system of each dislocation is obtained. In the case of thick samples and large dislocation densities, reconstruction from stereo pairs may still be the best option as it is less affected by the superposition of dislocations in the view plane.[13]

Besides, as a new technique it is still possible to optimize it in many ways. Linking it with transmission Kikuchi diffraction (TKD) for the determination of the crystal orientation may extend the applicability of this technique and improve the reconstruction accuracy; tracing of the dislocations from a STEM micrograph would increase the resolution. Tracing the dislocation from a micrograph where all features are visible can also be done, and the addition of slip along non-octahedral planes can easily be incorporated. Moreover, this technique could be applied to any crystal structure as long as the orientation of the appropriate planes can be determined.

## VI. CONCLUSION

A set of equations to acquire the crystal orientation of an SEM or TEM fcc sample was derived, which relies on measuring the angles that planar deformation features show on a 2D micrograph accounting for the tilt of the specimen. Examples with a known and an unknown sample orientation with respect to the electron beam were introduced and validated by electron microscopy in two nickel-based superalloys.

The orientation framework was then expanded into a technique for the 3D reconstruction of plastic deformation features with a planar nature from their 2D projections. Such features include perfect and dissociated dislocations, twin boundaries, and cross slip events,

although other dislocation structures containing nodes can also be incorporated. The steps to build such a model are:

– Determine the orientations of the crystal and the sample with respect to the electron beam.
– For each deformation feature determine its plane orientation and a pinning point where it intersects a sample surface or any other known point in order to obtain the equation of its slip plane.
– For each dislocation trace its $(x,y)$ coordinates and reproduce their 3D geometry from the equation of its slip plane.

This is the first methodology to reconstruct the true geometry of dislocations by tracing their coordinates on a single micrograph, and it allows for a better understanding of the mechanisms taking place in it. The manual task of identifying the adequate slip planes for each feature is the main limitation of this technique, but it can be overcome by analyzing multiple images of the same region taken at different orientations. Thus, it can complement a standard Burgers vector analysis without the need of taking any additional micrographs. Furthermore, this methodology could be extended to other crystal structures and features as long as the orientations of the corresponding planes are known.

## OPEN ACCESS

## ELECTRONIC SUPPLEMENTARY MATERIAL

The online version of this article (https://doi.org/10.1007/s11661-019-05595-1) contains supplementary material, which is available to authorized users.

## REFERENCES

1. S. Yamasaki, M. Mitsuhara, K. Ikeda, S. Hata, and H. Nakashima: *Scr. Mater.*, 2015, vol. 101, pp. 80–83.
2. G. Smith, D. Hudson, P. Styman, and C. Williams: *Philos. Mag.*, 2013, vol. 93, pp. 3726–40.
3. J.S. Barnard, J. Sharp, J.R. Tong, and P.A. Midgley: *J. Phys.*, 2006, vol. 26, pp. 247–50.
4. M. Tanaka, M. Honda, M. Mitsuhara, S. Hata, K. Kaneko, and K. Higashida: *Mater. Trans.*, 2008, vol. 49, pp. 1953–56.
5. G. Liu and I. Robertson: *J. Mater. Res.*, 2011, vol. 26, pp. 514–22.
6. C.-C. Chen, C. Zhu, E.R. White, C.-Y. Chiu, M.C. Scott, B.C. Regan, L.D. Marks, Y. Huang, and J. Miao: *Nature*, 2013, vol. 496, pp. 74–77.
7. S. Hata, K. Sato, M. Murayama, T. Tsuchiyama, and H. Nakashima: *ISIJ Int.*, 2015, vol. 55, pp. 623–31.
8. J.H. Sharp, J.S. Barnard, K. Kaneko, K. Higashida, and P.A. Midgley: *J. Phys.*, 2008, vol. 126, p. 012013.
9. E. Oveisi, A. Letouzey, D.T.L. Alexander, Q. Jeangros, R. Schäublin, G. Lucas, P. Fua, and C. Hébert: *Sci. Rep.*, 2017, vol. 7, art. no. 10630.
10. B. Hudson: *J. Microsc.*, 1973, vol. 98, pp. 396–401.
11. L. Agudo Jácome, G. Eggeler, and A. Dlouhý: *Ultramicroscopy*, 2012, vol. 122, pp. 48–59.
12. R.J. McCabe, A. Misra, T.E. Mitchell, and K.B. Alexander: *Microsc. Microanal.*, 2003, vol. 9, pp. 29–35.
13. L. Agudo Jácome, K. Pöthkow, O. Paetsch, and H. Hege: *Ultramicroscopy*, 2018, vol. 195, pp. 157–70.
14. N. Thompson: *Proc. Phys. Soc. B*, 1953, vol. 66, pp. 481–92.
15. N. Bali: *Golden Co-ordinate Geometry*, 1st ed., Laxmi Publications, New Delhi, 2008.
16. D.B. Williams and C.B. Carter: *Transmission Electron Microscopy: A Textbook for Materials Science. Part 3: Imaging*, 2nd ed., Springer, New York, 2009.
17. F. León-Cázares, R. Schlütter, T. Jackson, E. Galindo-Nava, and C. Rae: *Acta Mater.*, 2019, vol. 182, pp. 47–59.
18. C. Kienl: Hot forging of the nickel-base superalloy ATI 718Plus. Ph.D. thesis, University of Cambridge, 2019.

**Publisher's Note** Springer Nature remains neutral with regard to jurisdictional claims in published maps and institutional affiliations.